scientific reports

Check for updates

OPEN

Identification of the pathological subtypes of lung cancer brain metastases with multiparametric MRI radiomics: A feasibility study

Lian-Yu Sui[1], Shuai Quan[2], Li-Hong Xing[1,2], Yu Zhang[1,2], Huan Meng[2], Jia-Liang Ren[2], Jia-Ning Wang[2,3]✉ & Xiao-Ping Yin[2,3]✉

This study was aimed at differentiating brain metastases (BMs) from non-small cell lung cancer (NSCLC) vs. small cell lung cancer (SCLC), and the adenocarcinoma (AD) vs. non-adenocarcinoma (NAD) subtypes, according to radiomics features derived from multiparametric magnetic resonance imaging (MRI). A total of 276 patients with BMs, including 98 with SCLC and 178 with NSCLC, were randomly divided into training (193 cases) and test (83 cases) datasets in a 7:3 ratio. Of the 178 patients with NSCLC, 155 had primary AD, and 23 had NAD; those patients were also randomly divided into training (124 cases) and test (54 cases) datasets. Logistic regression analysis was used to construct classification models based on the radiomics features extracted from contrast-enhanced T1-weighted imaging (T1CE), T2-fluid-attenuated inversion recovery (T2-FLAIR), and diffusion-weighted imaging (DWI) images. Diagnostic efficiency was evaluated with the area under the receiver operating characteristic curve (AUC) through Delong's test, calibration curves through the Hosmer-Lemeshow test and Brier score, precision-recall curves, and decision curve analysis. Compared with radiomics features derived from a single sequence, multiparametric combined-sequence MRI radiomics features based on T1CE, T2-FLAIR, and DWI images exhibited greater specificity in distinguishing BMs originating from various lung cancer subtypes. In the training and test datasets, the AUCs of the model for the classification of SCLC and NSCLC BMs were 0.765 (95% CI 0.711, 0.822) and 0.762 (95% CI 0.671, 0.845), respectively, whereas the AUCs of the prediction models combining the three sequences in differentiating AD from NAD BMs were 0.861 (95% CI 0.756, 0.951) and 0.851 (95% CI 0.649, 0.984), respectively. The radiomics classification method based on the combination of multiple MRI sequences can be used for differentiating various lung cancer BMs.

Keywords Lung cancer, Brain metastases, Radiomics, Magnetic resonance imaging, Pathology

Abbreviations

BMs	Brain metastases
SCLC	Small cell lung cancer
NSCLC	Non-small cell lung cancer
AD	Adenocarcinoma
NAD	Non-adenocarcinoma
CT	Computed tomography
PET	Positron emission tomography
MRI	Magnetic resonance imaging
T1CE	Contrast-enhanced T1 weighted imaging
T1WI	T1 weighted imaging
T2-FLAIR	T2-fluid-attenuated inversion recovery
DWI	Diffusion-weighted imaging

[1]Affiliated Hospital of Hebei University/School of Clinical Medicine of Hebei University, Baoding, China. [2]Department of Radiology, Hebei Key Laboratory of Precise Imaging of Inflammation Related Tumors, the Affiliated Hospital of Hebei University, 212 Eastern Yuhua Road, Baoding City 071000, Hebei Province, China. [3]Department of Radiology, Affiliated Hospital of Hebei University, No. 212 of yuhua East Road, lianchi District, Baoding 071002, China. ✉email: jianingwang06@outlook.com; yinxiaoping78@sina.com

ROC	Receiver operating characteristic curve
AUC	Area under the receiver operating characteristic curve
ACC	Accuracy
SEN	Sensitivity
SPE	Specificity
PPV	Positive predictive value
NPV	Negative predictive value
Std	Standard deviation
CI	Confidence intervals
TR	Repetition time
TE	Echo time
NSA	Number of signal averages
FOV	Field of view
ICC	Intraclass correlation coefficient
ROI	Region of interest
HL	Hosmer-Lemeshow
BS	Brier score

Brain metastases (BMs) develop as secondary malignant tumors stemming from solid organ cancers outside the central nervous system. BMs are increasing in incidence, and they cause substantial morbidity and mortality, because of their heterogeneous features and frequent late stage diagnosis[1]. Lung cancer, the main origin of primary tumors that give rise to BMs, is responsible for nearly 50% of BMs[2]. The most common lung cancer type is non-small cell lung cancer (NSCLC), accounting for approximately 90%, whereas the remainder of cases are small cell lung cancer (SCLC)[3]. The main histological subtype of NSCLC is adenocarcinoma (AD)[4]. Given the multiple treatment options available for patients with BMs from lung cancer, a reliable classification of histopathological types is highly desirable to enable early and individualized management[5]. Invasive biopsy and histopathological workup are generally required for accurate diagnosis. However, contraindications to surgical lung resection and the limitations of BM biopsies make diagnosis challenging for clinicians. Furthermore, most BMs are diagnosed through magnetic resonance imaging (MRI) scans[6]. Hence, the ability to infer lung cancer pathological type through the MRI findings for BMs would have great clinical value.

Cross-sectional MRI is indispensable for BM diagnosis and treatment, yet it is currently applied only at the macroscopic level and is limited primarily to subjective observation. Radiomics can extract many quantitative image features from high-quality, standardized medical images through high-throughput feature extraction methods. These features reflect tumors' microstructure and biological behavior[7]. Compared with the relatively limited information provided by traditional MRI diagnostic methods, radiomics offers rich information on tumor phenotypes, and can quantify image features that are imperceptible to humans, thus extensively revealing tumor heterogeneity. This method has broad application prospects for differential diagnosis, pathological classification, and non-invasive characterization of molecular subtypes of lung cancer BMs, thereby facilitating individualized precision treatment for tumors[8–10]. Previous studies have demonstrated the feasibility of radiomics in classifying various pathological types of lung cancer according to histopathological information. However, those studies have relied solely on primary lung cancer or computed tomography (CT) radiomics[11–13]. MRI radiomics, as a "virtual biopsy" approach, correlates MRI image features with histopathological changes, and consequently can address challenges that are difficult or impossible for radiologists to solve through viewing with the naked eye alone[14].

By extracting high-throughput features from multiparametric brain MRI to reflect the heterogeneity of tumor lesions, radiomics can help guide the pathological classification of lung cancer BMs, thereby providing new ideas for the diagnosis and treatment management of lung cancer BMs. This modality simplifies the diagnosis and treatment process, decreases patient burden, and aids in the development of personalized treatment plans for patients who cannot undergo invasive histopathological examinations. The integration of radiomics, a rapid and non-invasive pathological classification tool, into clinical practice has great potential for enhancing clinical decision-making. Therefore, this article is aimed at demonstrating that a radiomics method of step-wise binary classification based on multiparametric MRI can distinguish various pathological subtypes of BMs in lung cancers including SCLC, NSCLC, AD, and non-adenocarcinoma (NAD). Our findings provide a potential analytical approach for personalized diagnostic and therapeutic decision-making.

Materials and methods

Patients

This retrospective study was approved by the Research Ethics Committee of the Affiliated Hospital of Hebei University, and all methods were performed in accordance with the relevant guidelines and regulations. Requirements for informed consent were waived by the Research Ethics Committee of the Affiliated Hospital of Hebei University. Between January 2016 and June 2019, MRIs for patients with lung cancer BMs were collected at our hospital. All enrolled patients underwent brain MRI examinations. The inclusion criteria were as follows: (1) all BMs were confirmed through pathology, imaging, and clinical follow-up; (2) the diagnosis of primary lung cancer and its histological differentiation into SCLC, AD, or NAD were confirmed through biopsy or surgery; and (3) complete MRI scan sequences were available, including contrast-enhanced T1-weighted imaging (T1CE), T2-fluid-attenuated inversion recovery (T2-FLAIR), and diffusion-weighted imaging (DWI). The exclusion criteria comprised (1) presence of other primary malignant tumors; (2) history of craniocerebral surgery; (3) incomplete clinical data for the patient; (4) poor MRI quality; and (5) incomplete T1CE, T2-FLAIR, or DWI brain MRI.

The flowchart for patient selection is shown in Fig. 1. This study was divided into two stepwise parts: part I distinguished BMs from NSCLC vs. SCLC, whereas part II identified BMs from AD vs. NAD within NSCLC. To simulate real-world clinical practice, we randomly allocated patients to training and test datasets to evaluate the performance of the model. In part I (NSCLC vs. SCLC), patients were randomly assigned to the training dataset ($n = 193$) and the test dataset ($n = 83$) in a ratio of 7:3. In part II (AD vs. NAD), patients were also randomly assigned to the training set ($n = 124$) and the test set ($n = 54$) in a 7:3 ratio.

MRI protocol

All patients underwent brain MRI with one of the three MRI scanners (Siemens Amira 1.5 T, Philips Achieva 1.5 T, or GE Discovery MR750 3.0 T) at our hospital. Gadodiamide served as the contrast agent for cranial MRI. A high-pressure syringe was used to inject 0.01 mmol/kg (0.2 mL/kg) contrast through the cubital vein at an injection rate of 2 mL/s.

The typical scanning parameters for a 3 Tesla (T) machine scan were as follows:

- Transverse T1CE: repetition time (TR)/echo time (TE) (ms) = 2320/80, number of signal averages (NSA) = 1, field of view (FOV) = 21 cm × 32 cm, thickness/gap (mm) = 5.0/1.0.
- Transverse T2-FLAIR: TR/TE (ms) = 8000/109, NSA = 1, FOV = 24 cm × 36 cm, thickness/gap (mm) = 5.0/1.0.

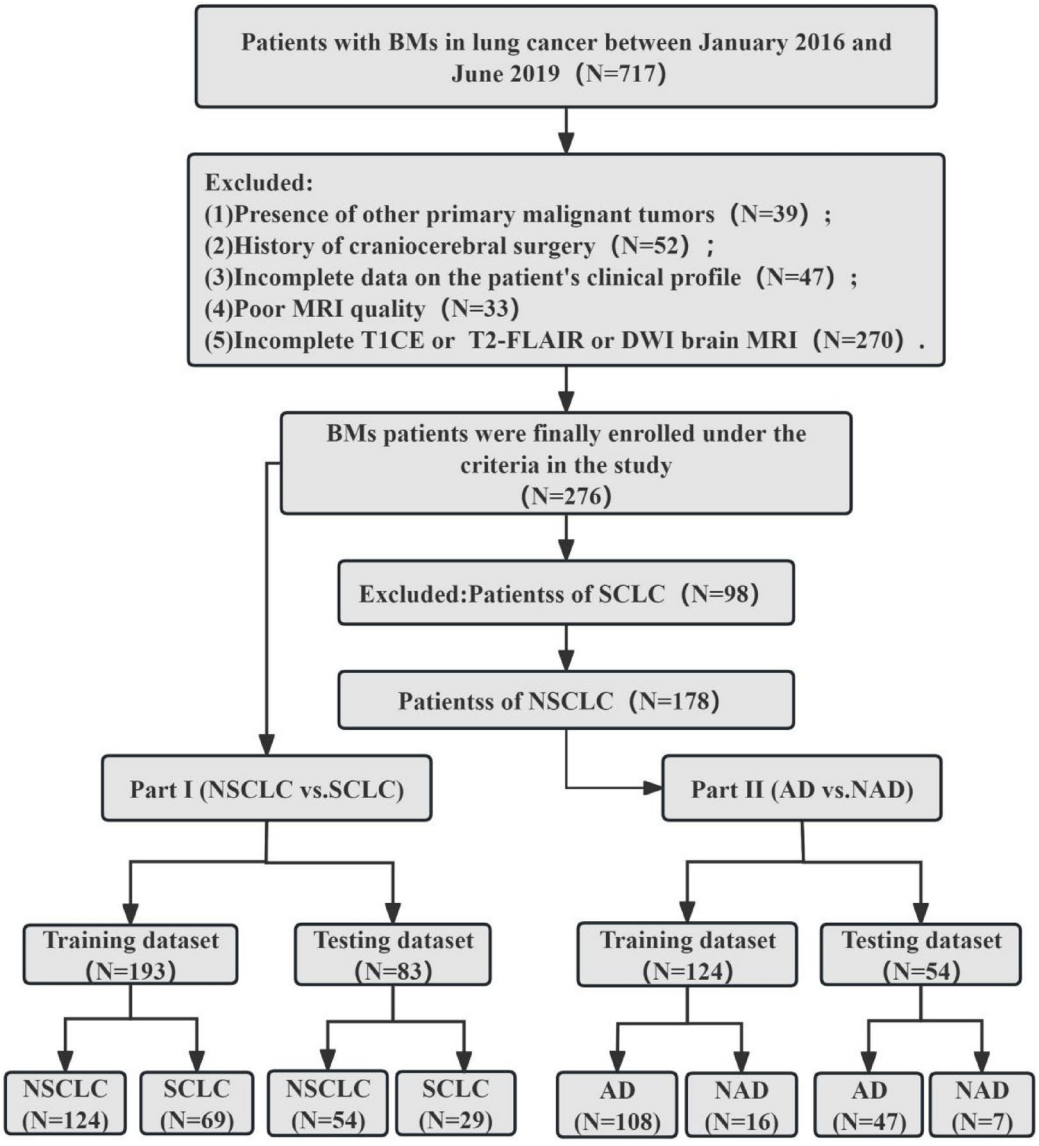

Fig. 1. Flowchart of patient selection for this retrospective study. T1CE, contrast-enhanced T1 weighted imaging; T2-FLAIR, T2-fluid-attenuated inversion recovery; DWI, diffusion-weighted imaging; BMs, brain metastases; SCLC, small-cell lung cancer; NSCLC, non-small-cell lung cancer; NAD, non-adenocarcinoma; AD, adenocarcinoma.

- Transverse DWI: TR/TE (ms) = 1,306/54, NSA = 2, FOV = 24 cm × 36 cm, thickness/gap (mm) = 5.0/1.0, B value selected 800 s/mm^2.

Tumor segmentation

The images were exported into Digital Imaging and Communications in Medicine format. All cases in the training cohort were used to train the predictive models, whereas cases in the test cohorts were used to independently evaluate model performance. Before analyses, in ITK-SNAP (version 3.8.0, www.itksnap.org) software, the entire volume of the region of interest (ROI) was manually contoured slice by slice along the boundaries of the tumor on T1CE, T2-FLAIR, and DWI images, by a radiologist with 5 years of diagnostic experience[15]. The segmentation process was supervised by a senior radiologist with 10 years of experience, to ensure the accuracy of the delineations. To ensure that the evaluation process was as unbiased as possible, and that the results were representative, the two assessors were fully blinded to the patients' pathological diagnoses. Figure 2(a1–2, b1–2, c1–2, d1–2, e1–2, f1–2, g1–2, h1–2, i1–2) shows the ROI ranges for patients with SCLC, AD, and NAD with BMs.

Feature extraction and selection

Figure 3 presents a concise workflow of this study. The image preprocessing steps were based on prior research and adhered to the Image Biomarker Standardization Initiative guidelines[16]. Given that multiple similar lesions might have existed in the same patient, to avoid redundant feature extraction based on the lesion level, we focused on the largest lesion area at the case level, thus enabling the model to focus on the most prominent and representative features contributing to the classification tasks.

First, because the original images were obtained from different MRI scanners, image pre-processing was performed before feature extraction. The MRI intensity values were standardized with the z-score method, and the gray values of the images were adjusted to a standard normal distribution to eliminate the influence of dimensionality and ensure comparability among different features. Subsequently, the pre-processed images and corresponding contoured target ROIs were imported into artificial intelligence software (version 3.3.0, Artificial Intelligence Kit, GE Healthcare, China) for the extraction of radiomics features from each ROI of every sequence, including T1CE, T2-FLAIR, and DWI. Each set of 1,037 features for each sequence of each case was extracted from the original images, including shape features, first-order intensity features, textural features (gray-level cooccurrence matrix, gray-level run-length matrix, and gray-level size zone matrix), and high-order wavelet features. Ultimately, a total of 3,111 radiomics features were extracted for each patient[17].

To prevent overfitting problems, radiomics features must be screened. To mitigate overfitting, we applied data augmentation techniques to the image patches, including horizontal flipping, vertical flipping, and random rotation, thereby increasing the diversity and variability of the training data. Subsequently, through cross-validation, after each division of the data set, feature selection algorithms were used on the training set to select

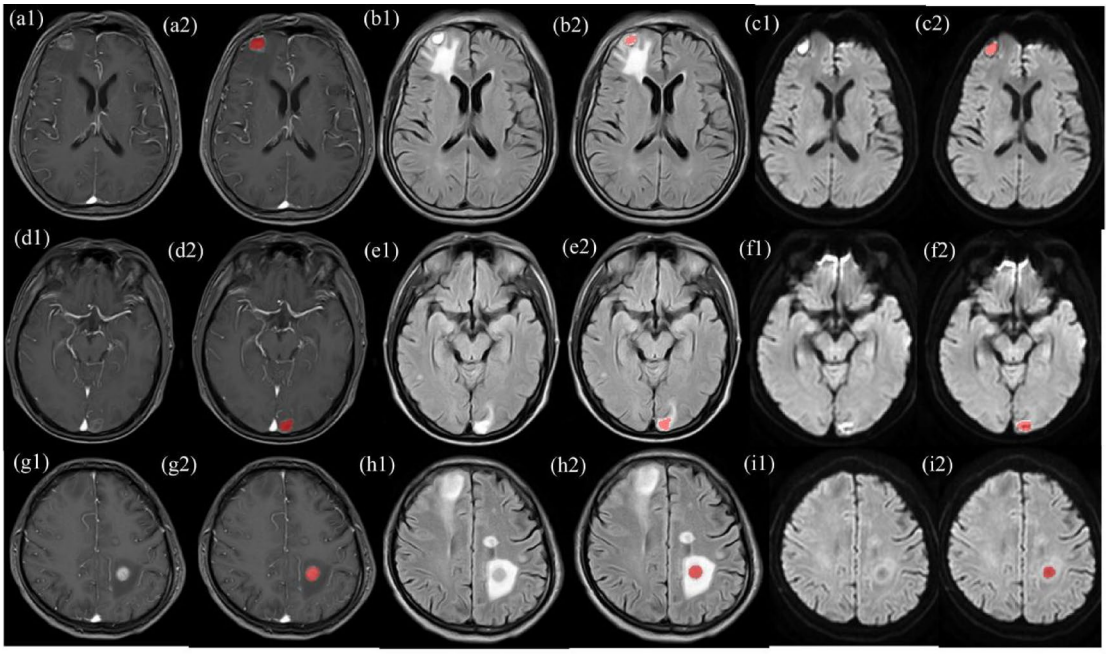

Fig. 2. Delineation of ROIs in T1-weighted imaging (T1WI) (a1–2, d1–2, g1–2), T2-fluid-attenuated inversion recovery (T2-FLAIR) (b = 800) (b1–2, e1–2, h1–2), and diffusion-weighted imaging (DWI) (c1–2, f1–2, i1–2). a1–2, b1–2, c1–2: man, 66 years old, with BMs in SCLC. a1, b1, and c1 represent the original lesions, and a2, b2, and c2 show the lesions after ROI delineation. d1–2, e1–2, f1–2: man, 45 years old, with BMs in AD. d1, e1, and f1 represent the original lesions, and d2, e2, and f2 depict the lesions after ROI delineation. g1–2, h1–2, i1–2: man, 49 years old, with BMs i*n NAD*. g1, h1, and i1 represent the original lesions, and g2, h2, and i2 display the lesions after ROI delineation.

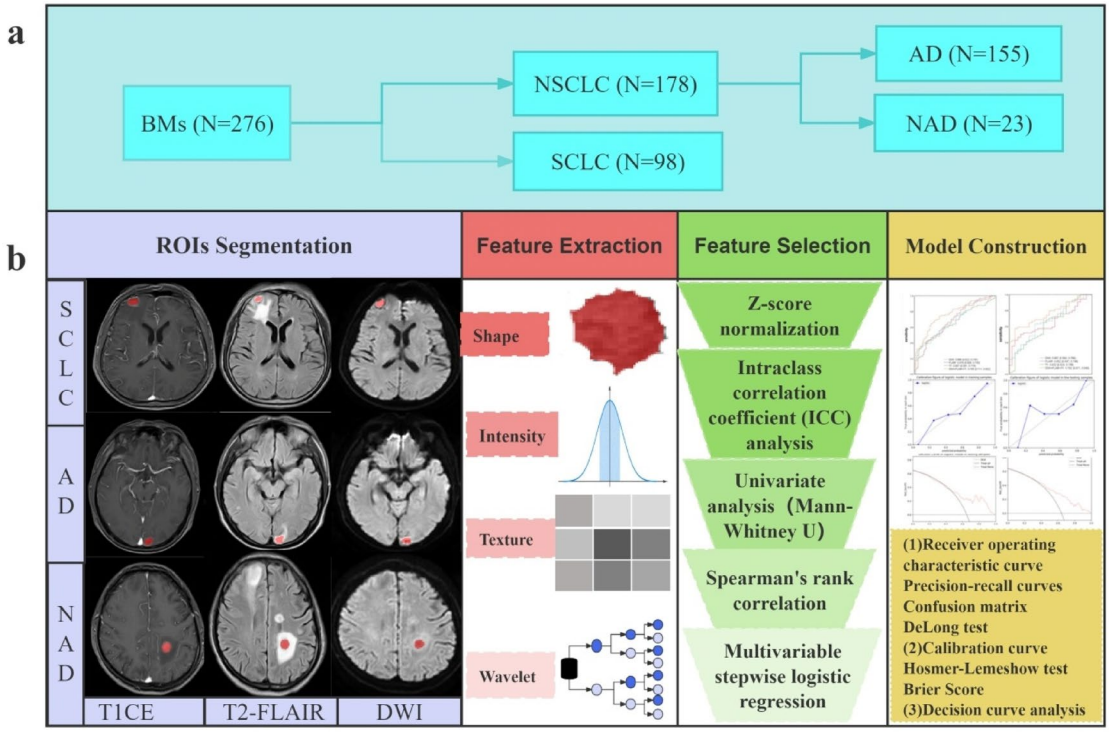

Fig. 3. Brief study workflow. Two-level stepwise architecture for the classification of the metastatic tumor types of BMs (**a**). Flowchart of radiomics analyses (**b**). T1CE, contrast-enhanced T1 weighted imaging; T2-FLAIR, T2-fluid-attenuated inversion recovery; DWI, diffusion-weighted imaging; BMs, brain metastases; SCLC, small-cell lung cancer; NAD, non-adenocarcinoma; AD, adenocarcinoma.

features. The performance of the models constructed with these features was evaluated on the test set. Through these multiple processes, unstable features that performed well only on specific data subsets were eliminated, whereas the retained features were likely to possess universal predictive abilities.

Radiomics features with high correlation and low redundancy were selected through intraclass correlation coefficient (ICC) analysis. Features with low confidence coefficients were excluded, and only those with ICC ≥ 0.8 were retained for further analysis. First, the Mann-Whitney U test was used to compare radiomics features between two independent groups, because the ROIs were manually delineated by two radiologists and did not overlap. The radiomics features with a P value < 0.05 from the univariate logistic analysis were preliminarily retained by the Mann-Whitney U test to identify significant features. Subsequently, according to the Spearman correlation coefficients generated in correlation analysis, the stable radiomics features with characteristic parameters greater than 0.9 were eliminated to ensure robustness. Finally, multivariable logistic regression was used to determine the optimal features, with the Akaike information criterion as the threshold[18].

Binary classification model construction

Images from three MRI sequences (T1CE, DWI, and T2-FLAIR) were used to build corresponding prediction radiomics models with logistic regression analysis based on optimal radiomics parameters. These models were the T1CE model, the DWI model, the T2-FLAIR model, and multi-sequence model. Because prior studies on metastatic typing of BMs have demonstrated that stepwise binary classification models outperform one-step multiclass models—probably because their simple, straightforward characteristics enable them to focus on distinguishing one category from another, and more effectively correctly identify categories and minimizing classification errors—we used the former approach in our study[19]. The binary classification model constructed for SCLC vs. NSCLC and AD vs. NAD in this study consisted of two parts based on the same structure, with the inputs to the radiomics models comprising preprocessed T1CE, T2-FLAIR, and DWI image patches. Each part included the T1CE model, the DWI model, the T2-FLAIR model, and the multisequence model.

For each logistic model, discrimination performance was calculated with the area under the receiver operating characteristic curve (AUC), and Delong's test was performed to compare the differences between AUCs, and various other diagnostic indices, including accuracy (ACC), sensitivity (SEN), specificity (SPE), positive predictive value (PPV), and negative predictive value (NPV). Moreover, precision-recall curves and confusion matrices served as complementary tools for comprehensively understanding the performance of classification models, thus facilitating informed decisions regarding model selection and optimization. Additionally, the Youden index was used to determine the optimal cut-off value maximizing the sum of sensitivity and specificity. The ICC was used to assess the reproducibility of radiomics features, both within and between observers. The calibration curve, alongside the Hosmer-Lemeshow (HL) test and Brier score (BS), was applied to describe the

Characteristics	Training dataset (*N* = 193)			Test dataset (*N* = 83)			Overall (*N* = 276)		
	NSCLC	SCLC	*P* value[a]	NSCLC	SCLC	*P* value[b]	NSCLC	SCLC	*P* value[a]
Number of patients (N,%)	124(64.2)	69(35.8)		54(65.1)	29(34.9)		178(64.5)	98(35.5)	
Age (mean ± std, years)	59.9 ± 10.2	63.7 ± 7.5	0.137	62.7 ± 7.5	57.0 ± 13.0	0.267	60.78 ± 9.2	61.47 ± 9.1	0.070
Sex (N,%)			0.333			0.341			0.128
Female	80(64.5)	47(68.1)		29(53.7)	22(75.9)		109(61.2)	69(70.4)	
Male	44(35.5)	22(31.9)		25(46.3)	7(24.1)		69(38.8)	29(29.6)	
Tobacco use (N,%)			0.196			0.298			0.050
Nonsmoker	49(39.5)	38(55.1)		25(46.3)	17(58.6)		74(41.6)	55(56.1)	
Smoker	75(60.5)	31(44.9)		29(53.7)	12(41.4)		104(58.4)	43(43.9)	
Clinical stage (N,%)			0.145			0.385			< 0.001*
IVA	25(20.2)	40(58.0)		22(40.7)	15(51.7)		47(26.4)	55(56.1)	
IVB	99(79.8)	29(42.0)		32(59.3)	14(48.3)		131(73.6)	43(43.9)	

Table 1. Clinical characteristics of patients with BMs from NSCLC and SCLC in the training and test datasets. Note: BMs, brain metastases; SCLC, small-cell lung cancer; NSCLC, non-small-cell lung cancer. [a] Wilcoxon rank sum test, Pearson's chi-squared test; [b] Wilcoxon rank sum exact test, Pearson's chi-squared test; *, P value < 0.05.

Characteristics	Training dataset (*N* = 124)			Test dataset (*N* = 54)			Overall (*N* = 178)		
	AD	NAD	*P* value[a]	AD	NAD	*P* value[b]	AD	NAD	*P* value[a]
Number of patients (N,%)	108(87.1)	16(12.9)		47(87.0)	7(13.0)		155(87.1)	23 (12.9)	
Age (mean ± std, years)	60.4 ± 9.5	62.4 ± 12.4	0.247	60.8 ± 8.8	561.6 ± 4.2	0.331	60.54 ± 9.2	62.4 ± 12.4	0.464
Sex (N, %)			0.234			0.239			< 0.001*
Female	57(52.8)	15(93.8)		30(63.8)	7(100)		87(56.1)	22(95.6)	
Male	51(47.2)	1(6.2)		17(36.2)	0(0)		68(43.9)	1(4.4)	
Tobacco use (N, %)			0.279			0.142			0.718
Nonsmoker	66(39.5)	10(55.1)		29(46.3)	5(58.6)		95(61.3)	15(65.2)	
Smoker	42(60.5)	6(44.9)		18(53.7)	2(41.4)		60(38.7)	8(34.8)	
Clinical stage (N, %)			0.218			0.218			0.405
IVA	68(20.2)	9(58.0)		27(40.7)	3(51.7)		95(61.3)	12(52.2)	
IVB	40(79.8)	7(42.0)		20(59.3)	4(48.3)		60(38.7)	11(47.8)	

Table 2. Clinical characteristics of patients with BMs from NAD and AD in the training and test datasets. Note: BMs, brain metastases; NAD, non-adenocarcinoma; AD, adenocarcinoma. [a] Wilcoxon rank sum test, Pearson's chi-squared test; [b] Wilcoxon rank sum exact test, Pearson's chi-squared test; *, P value < 0.05.

agreement between radiomics model prediction and actual pathological classification, wherein a significant test statistic indicated imperfections in the model's calibration. Finally, decision curve analysis was used to evaluate the effectiveness of the radiomics model, and assess the clinical utility and practical value of the predictive signatures[19,20].

Statistical analysis

The clinical data for enrolled patients were analyzed in R Statistical Software (version 3.6.3 available at www.rproject.org). For all tests, the significance threshold for differences was set at $P < 0.05$. Continuous variables (age) are presented as mean ± standard deviation, and 95% confidence intervals (CIs) were also calculated. The differences in clinical characteristics between the training and the test datasets were compared with the Mann-Whitney U test for continuous variables (age) and the chi-square test for categorical variables (sex, tobacco use, and clinical stage). In radiomics analysis, the ICC was used to evaluate the intra- and interobserver reproducibility of radiomics features, and DeLong's test was used to compare the AUCs among models.

Results

Patients' clinical characteristics

A total of 276 patients with BMs, admitted between June 2016 and June 2021, were reviewed. Of these, 178 had primary NSCLC, and 98 had SCLC. Of the 178 patients with NSCLC, 155 had AD, and 23 had NAD. Tables 1 and 2 show the clinical characteristics of the enrolled patients and their division into training and test datasets, classified according to the individual tumors. The training and test datasets showed no statistically significant differences in age, sex, tobacco use, and clinical stage. In the overall datasets, clinical stage ($P < 0.001$) between NSCLC and SCLC and age ($P < 0.001$) between NAD and AD showed statistically significant differences.

Number	Radiomics features	Sequences	*P* value	[0.025,0.975]
1	original_shape_SurfaceVolumeRatio	T1CE	0.0300	[0.0200, 0.0500]
2	wavelet-HLL_glcm_Correlation	T1CE	0.0100	[0.0050, 0.0200]
3	log-sigma-3-0-mm-3D_firstorder_Skewness	T1CE	0.0450	[0.0200,0.0700]
4	wavelet-LLH_glszm_LowGrayLevelZoneEmphasis	T1CE	0.0200	[0.0100,0.0400]
5	wavelet-HHH_glszm_SmallAreaLowGrayLevelEmphasis	T2-FLAIR	0.0080	[0.0030,0.0200]
6	wavelet-HLL_firstorder_Skewness	T2-FLAIR	0.0490	[0.0200,0.0800]
7	wavelet-HHL_glrlm_RunEntropy	T2-FLAIR	0.0320	[0.0100,0.0600]
8	wavelet-LLL_glcm_Autocorrelation	DWI	0.0120	[0.0050,0.0300]
9	wavelet-HLH_glcm_MaximumProbability	DWI	0.0053	[-0.1726,0.9901]
10	original_gldm_SmallDependenceHighGrayLevelEmphasis	DWI	0.0000	[-2.6970,-1.4954]
11	log-sigma-3-0-mm-3D_ngtdm_Busyness	DWI	0.0145	[-0.1931,1.7588]

Table 3. List of selected radiomics features in differentiating between NSCLC and SCLC BMs. Note: T1CE, contrast-enhanced T1 weighted imaging; T2-FLAIR, T2-fluid-attenuated inversion recovery; DWI, diffusion-weighted imaging; BMs, brain metastases; SCLC, small-cell lung cancer; NSCLC, non-small-cell lung cancer.

Models	Training dataset				Test dataset			
(95%CI)	T1CE	FLAIR	DWI	T1CE + FLAIR + DWI	T1CE	FLAIR	DWI	T1CE + FLAIR + DWI
AUC	0.657 (0.591,0.719)	0.676 (0.608,0.743)	0.686 (0.622,0.747)	0.765 (0.711,0.822)	0.632 (0.524,0.738)	0.652 (0.547,0.748)	0.667 (0.564,0.766)	0.762 (0.671,0.845)
ACC	0.570 (0.485,0.655)	0.570 (0.485,655)	0.539 (0.454,0.624)	0.694 (0.629, 0.759)	0.530 (0.421,0.639)	0.627 (0.518,0.736)	0.506 (0.397,0.615)	0.675 (0.566, 0.784)
SEN	0.407 (0.298,0.516)	0.570 (0.461,0.679)	0.315 (0.216,0.414)	0.694 (0.605, 0.783)	0.407 (0.293,0.521)	0.627 (0.513,0.741)	0.296 (0.182,0.410)	0.648 (0.534, 0.762)
SPE	0.899 (0.856,0.942)	0.855 (0.802,0.908)	0.942 (0.909,0.975)	0.797 (0.744, 0.850)	0.759 (0.650,0.868)	0.862 (0.753,0.971)	0.897 (0.788,1.006)	0.724 (0.615, 0.833)
PPV	0.873 (0.789,0.957)	0.836 (0.752,0.920)	0.907 (0.843,0.971)	0.849 (0.775, 0.923)	0.759 (0.640,0.878)	0.871 (0.762,0.980)	0.842 (0.723,0.961)	0.814 (0.695, 0.933)
NPV	0.449 (0.354,0.544)	0.447 (0.352,0.542)	0.433 (0.338,0.528)	0.550 (0.455, 0.645)	0.407 (0.293,0.521)	0.481 (0.367,0.595)	0.406 (0.292,0.520)	0.525 (0.411, 0.639)

Table 4. Model performance comparison for the three individual and combined MRI sequences in differentiating between NSCLC and SCLC BMs. Note: T1CE, contrast-enhanced T1 weighted imaging; T2-FLAIR, T2-fluid-attenuated inversion recovery; DWI, diffusion-weighted imaging; BMs, brain metastases; SCLC, small-cell lung cancer; NSCLC, non-small-cell lung cancer; CI, confidence intervals.

Classification of performance of the radiomics models

Two-level stepwise binary logistic regression classifiers were constructed to predict metastatic types of BMs in lung cancer: the first was used to differentiate SCLC from NSCLC, whereas the second was used to differentiate AD from NAD within NSCLC. The binary classification models were effective in correctly identifying classes and minimizing errors (NSCLC vs. SCLC, and AD vs. NAD).

Performance assessment of NSCLC and SCLC

A total of 11 radiomics features, comprising four, three, and four features from T1CE, T2-FLAIR, and DWI, respectively, were retained as the most valuable radiomics characteristics for constructing binary classification models for SCLC vs. NSCLC on individual sequences, and all three sequences in combination. Table 3 lists the performance of the selected most important radiomics features for predicting the metastatic tumor subtypes of BMs (SCLC vs. NSCLC). The radiomics features demonstrated varying statistical significance across sequences, and some features exhibited notable statistical differences.

The performance of logistic regression classifiers on three single-sequence models and their combinations in distinguishing BMs from various pathological lung cancer types is shown in Table 4. Figure 4 depicts the receiver operating characteristic curves (ROC), precision-recall curves, and confusion matrix for each model in the training and test datasets. As shown in Table 4, the individual sequences (T1CE, T2-FLAIR, and DWI) yielded AUCs ranging from 0.657 to 0.686 in the training and test cohorts. In our model, comparison of the three individual MRI sequences indicated no significant differences, and the AUC output of DWI on the test set was slightly better (0.667). The generated combination of T1CE + T2-FLAIR + DWI showed an overall improvement in AUCs (0.762 and 0.765), with respect to the three single sequence models in the training and test cohorts. The difference in AUCs among all three sequences and individual sequences reached significance (T1CE + T2-FLAIR + DWI vs. T1CE: P value = 0.028, T1CE + T2-FLAIR + DWI vs. FLAIR: P value = 0.032, and T1CE + T2-FLAIR + DWI vs. FLAIR: P value = 0.040). The precision-recall curves for the classification model, which incorporated all three sequences, revealed that the logistic model demonstrated outstanding classification

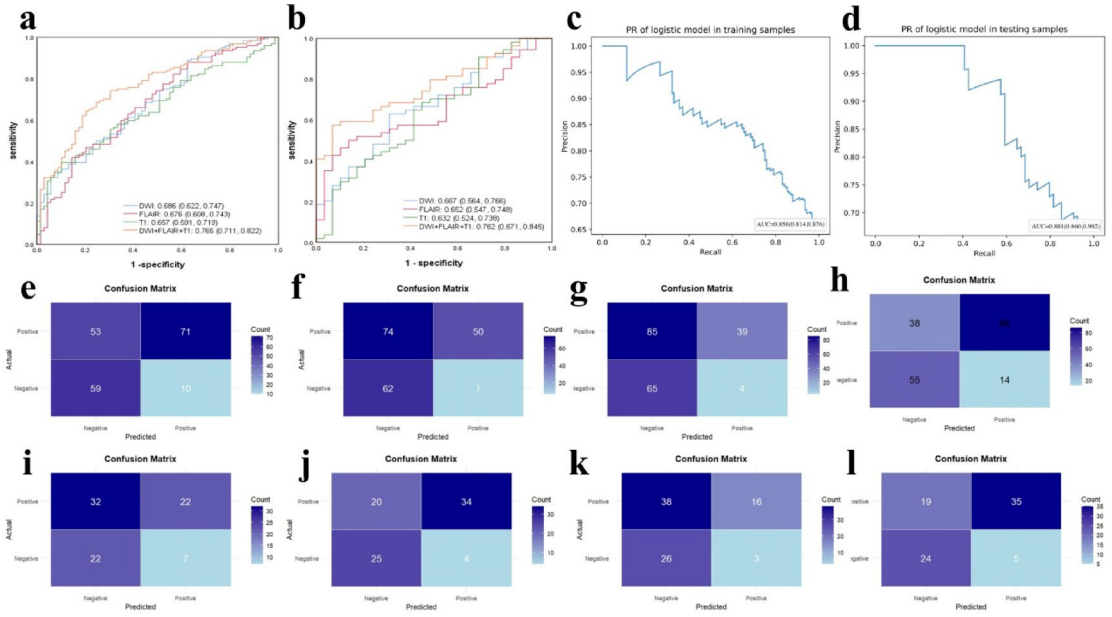

Fig. 4. ROC performance (**a**, **b**), precision-recall curves (**c**, **d**), and confusion matrix (**e–l**) for classifying NSCLC and SCLC BMs in the training (**a**, **c**, **e**, **f**) and test (**b**, **d**, **i–l**) cohorts. T1CE (**e**, **i**), FLAIR (**f**, **j**), DWI (**g**, **k**), and T1CE + FLAIR + DWI (**h**, **l**).

performance on both the training and test datasets, achieving AUC values exceeding 0.85. Notably, the AUC value for the test dataset (0.881) was marginally higher than that of the training set (0.858), thus indicating that the model exhibited slightly better performance on unseen data and demonstrated generalizability. Additionally, the confusion matrix provided supplementary visualization and interpretation of the performance of the radiomics models.

On the test set, the combination of all three sequences had an ACC of 0.675, SEN of 0.648, SPE of 0.724, PPV of 0.814, and NPV of 0.525. Furthermore, calibration curves for the probability of identifying NSCLC and SCLC in the training and test datasets exhibited robust concurrence between the observed and projected probabilities (Fig. 5a and b). The HL test and BS yielded insignificant deviations (training cohort: P value = 0.0.890, BS: 0.041; test cohort: P value = 0.764, BS: 0.097), thus indicating conformity. Decision curve analysis indicated the enhanced clinical benefit of the combination signature (Fig. 5c and d).

Performance assessment of AD and NAD

Table 5 lists the performance of the selected most significant radiomics across various sequences and their P values in predicting the metastatic tumor types of BMs (AD vs. NAD). The radiomics features exhibited differing statistical significance across sequences, and some features showed significant statistical differences in specific sequences. The AD vs. NAD classification models were constructed on the basis of eight optimal radiomics features obtained through feature extraction and selection from three sequences, comprising three from T1CE, two from T2-FLAIR, and three from DWI. A logistic regression classifier was used to perform the binary classification of individual sequences as well as their combinations.

Table 6 presents the performance of logistic regression classifiers across three individual single-sequence models, and their various combinations, for differentiation between AD and NAD. Figure 6 illustrates the ROC curves, precision-recall curves, and confusion matrix for each model in both the training and test datasets. From the results of three single sequences, we concluded that the T1CE model had the best prediction performance on the test dataset, with an AUC of 0.772 and ACC of 0.685. All three sequences outperformed on the combination of individual sequences. The difference in AUCs for the three combined sequences vs. the individual sequences reached significance (T1CE + T2-FLAIR + DWI vs. T1CE: P value = 0.019, T1CE + T2-FLAIR + DWI vs. FLAIR: P value = 0.046, and T1CE + T2-FLAIR + DWI vs. FLAIR: P value = 0.035). The precision-recall curves of the classification models for AD vs. NAD on all three sequences in combination indicated that the logistic model exhibited favorable classification performance in both training and test sets. The model's performance on the training set (AUC = 0.750) was superior to that on the test set (AUC = 0.665), thereby suggesting potential overfitting, possibly because of the imbalance between AD and NAD data, as well as the relatively small NAD sample size.

On the test dataset, the combination of three MRI sequences had an AUC of 0.851, ACC of 0.871, SEN of 0.857, SPE of 0.872, PPV of 0.500, and NPV of 0.976. Moreover, calibration curves depicted the calibration of the combined model in terms of the agreement between the predicted risks of differentiating AD from NAD and observed outcomes (Fig. 7a and b). The HL test and BS yielded insignificant deviations (training cohort: P value = 0.857, BS: 0.063; test cohort: P value = 0.801, BS: 0.073), thus indicating conformity. Decision curve analysis indicated the clinical utility of the predictive signatures (Fig. 7c and d).

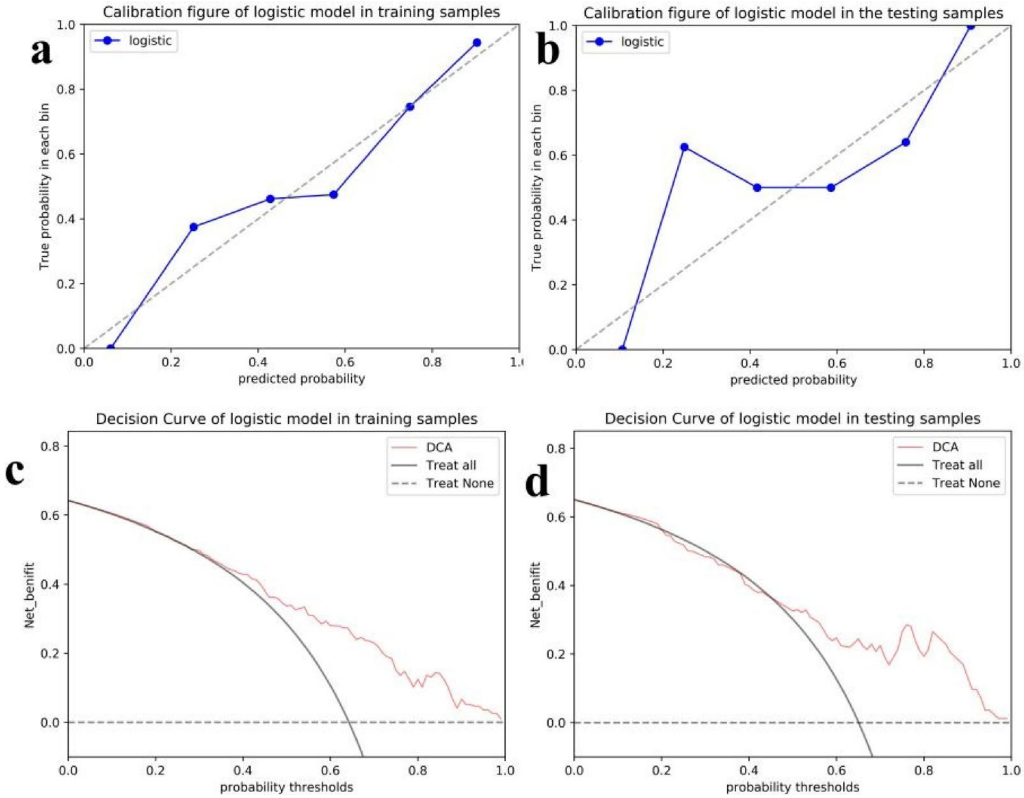

Fig. 5. Calibration curves (**a**, **b**) and decision curve analysis (**c**, **d**) of differentiating between NSCLC and SCLC BMs in the training cohort (**a**, **c**) and test cohort (**b**, **d**).

Number	Radiomics features	Sequences	*P* value	[0.025,0.975]
1	wavelet-HLH_glcm_InverseVariance	T1CE	0.0025	[-1.7284,0.3672]
2	log-sigma-5-0-mm-3D_gldm_DependenceNonUniformity	T1CE	0.01996	[-0.1470,0.7039]
3	wavelet-HHH_gldm_DependenceEntropy	T1CE	0.0140	[-0.1656,1.4681]
4	wavelet-HHH_gldm_DependenceEntropy	T2-FLAIR	0.0408	[0.0273,1.2816]
5	wavelet-HLH_glszm_LargeAreaLowGrayLevelEmphasis	T2-FLAIR	0.0101	[-0.8102,0.1095]
6	waveletHHH_gldm_LargeDependenceHighGrayLevelEmphasis	DWI	0.0063	[-0.1179,0.5459]
7	wavelet-HLL_ngtdm_Busyness	DWI	0.0062	[-0,1186,0.7182]
8	original_glcm_ClusterShade	DWI	0.0247	[-0.7556,0.0918]

Table 5. Selected radiomics features differentiating between AD and NAD BMs. Note: T1CE, contrast-enhanced T1 weighted imaging; T2-FLAIR, T2-fluid-attenuated inversion recovery; DWI, diffusion-weighted imaging; BMs, brain metastases; NAD, non-adenocarcinoma; AD, adenocarcinoma.

Discussion

The ability to type primary lung cancer according to MRI images of BMs would be highly advantageous to clinicians, particularly when conventional invasive procedures such as biopsies are difficult to perform. Brain MRI-based radiomics has been demonstrated to aid in noninvasive identification of the pathological subtypes of BMs in lung cancer[21]. In this study, we evaluated the feasibility of identifying the pathological types of BMs from lung cancer through a radiomics method. The multiparametric MRI-based radiomics achieved AUC values of 0.762 in the NSCLC vs. SCLC classification task and 0.851 in the AD vs. NAD classification task. Our results suggested that this radiomics model might serve as a noninvasive technique to predict metastatic tumor subtypes in patients with BMs with lung cancer, including those whose pathological subtypes remain unknown, thus potentially guiding the prioritization of diagnostic evaluations. Notably, such benefits are difficult for radiologists to achieve through visual inspection of preoperative brain MRI alone[22]. Our study provides evidence of the role of radiomics in complementing traditional imaging methods for the pathological subtypes of BMs in lung cancer. The collection of images from multiple MRI scanner models increased the heterogeneity of the data and enhanced the generalizability and clinical practicality of the model. However, we cannot rule out the possibility

Models	Training dataset				Test dataset			
(95%CI)	T1CE	FLAIR	DWI	T1CE + FLAIR + DWI	T1CE	FLAIR	DWI	T1CE + FLAIR + DWI
AUC	0.787 (0.676, 0.882)	0.768 (0.645, 0.877)	0.741 (0.635, 0.833)	0.861 (0.756, 0.951)	0.772 (0.558,0.944)	0.763 (0.618, 0.900)	0.733 (0.468,0.984)	0.851 (0.649, 0.984)
ACC	0.691 (0.621,0.761)	0.732 (0.662,0.802)	0.642 (0.572, 0.712)	0.821 (0.751, 0.891)	0.723 (0.653,0.793)	0.685 (0.615,0.755)	0.593 (0.523,0.663)	0.871 (0.801,0.941)
SEN	0.821 (0.751,0.891)	0.625 (0.555, 0.695)	0.750 (0.679,0.821)	0.750 (0.679, 0.821)	0.714 (0.644,0.784)	0.732 (0.662,0.802)	0.732 (0.662,0.802)	0.857 (0.787, 0.927)
SPE	0.776 (0.706, 0.846)	0.748 (0.678,0.818)	0.626 (0.556,0.696)	0.832 (0.762, 0.902)	0.745 (0.675,0.815)	0.681 (0.611,0.751)	0.574 (0.504,0.644)	0.872 (0.802, 0.942)
PPV	0.314 (0.244, 0.384)	0.270 (0.200,0.340)	0.231 (0.161,0.301)	0.400 (0.330, 0.470)	0.278 (0.208,0.348)	0.250 (0.180,0.320)	0.200 (0.130,0.270)	0.500 (0.430, 0.570)
NPV	0.943 (0.913,0.973)	0.930 (0.900,0.960)	0.944 (0.914,0.974)	0.957 (0.927, 0.987)	0.944 (0.914,0.974)	0.941 (0.911,0.971)	0.931 (0.901,0.961)	0.976 (0.956, 0.996)

Table 6. Model performance comparison for the three individual and combined MRI sequences in differentiating between AD and NAD BMs. Note: T1CE, contrast-enhanced T1 weighted imaging; T2-FLAIR, T2-fluid-attenuated inversion recovery; DWI, diffusion-weighted imaging; BMs, brain metastases; NAD, non-adenocarcinoma; AD, adenocarcinoma; CI, confidence intervals.

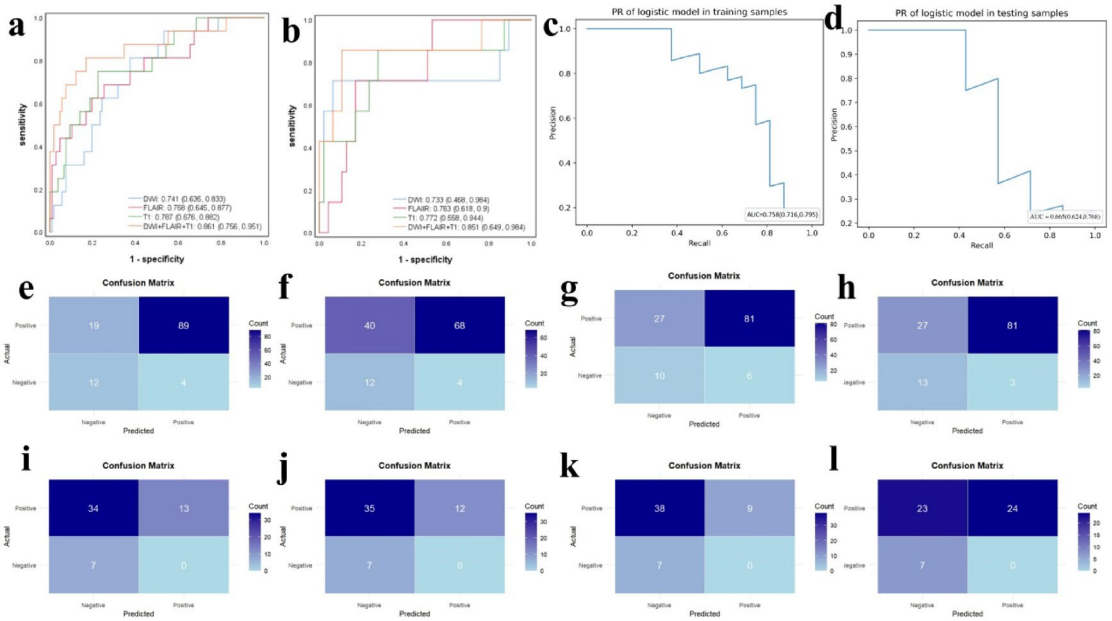

Fig. 6. Comparison of ROC curves (**a**, **b**), precision-recall curves (**c**, **d**), and confusion matrix (e–l) between the training (**a**, **c**, **e**, **f**) and test (**b**, **d**, **i–l**) datasets in differentiating between AD and NAD BMs. T1CE (**e**, **i**), FLAIR (**f**, **j**), DWI (**g**, **k**), and T1CE + FLAIR + DWI (**h**, **l**).

that the differences in scanning parameters due to the use of different MRI scanners might have influenced the overall robustness of the models to some extent.

Our study is novel in its analysis of MR images of BMs by using a radiomics method to classify lung cancer subtypes. Previous classifications of lung cancer through radiomics approaches have focused on primary tumors. For example, Tang et al.[23] have described the potential of multimodal chest MRI-based radiomics in discriminating between lung squamous cell carcinoma and AD subtypes of NSCLC. Their model achieved an AUC of 0.824 for the test dataset, a value comparable to those of CT or positron emission tomography (PET) based radiomics models in the identification of NSCLC subtypes[24,25]. Wang et al.[26] have demonstrated that the multi-parametric MR model has better predictive efficiency than CT and PET-based radiomics models. Our study indicated that imaging-based features of brain MRI might contain complementary information regarding the metastatic subtypes of BMs from lung cancer, thus advancing understanding in this field.

Herein, with integration of different MRI sequences, the combined model significantly improved the predictive capability and outperformed all individual sequence models. Studies have shown that DWI is highly valuable in BM evaluation and have demonstrated that most lung cancer BMs show hyperintensity on DWI[27]. Furthermore, current guidelines[28] recommend T1CE as an effective tool and important indicator in the diagnosis of BMs, representing destruction of the blood-brain barrier. Moreover, T2-FLAIR can best detect peritumoral

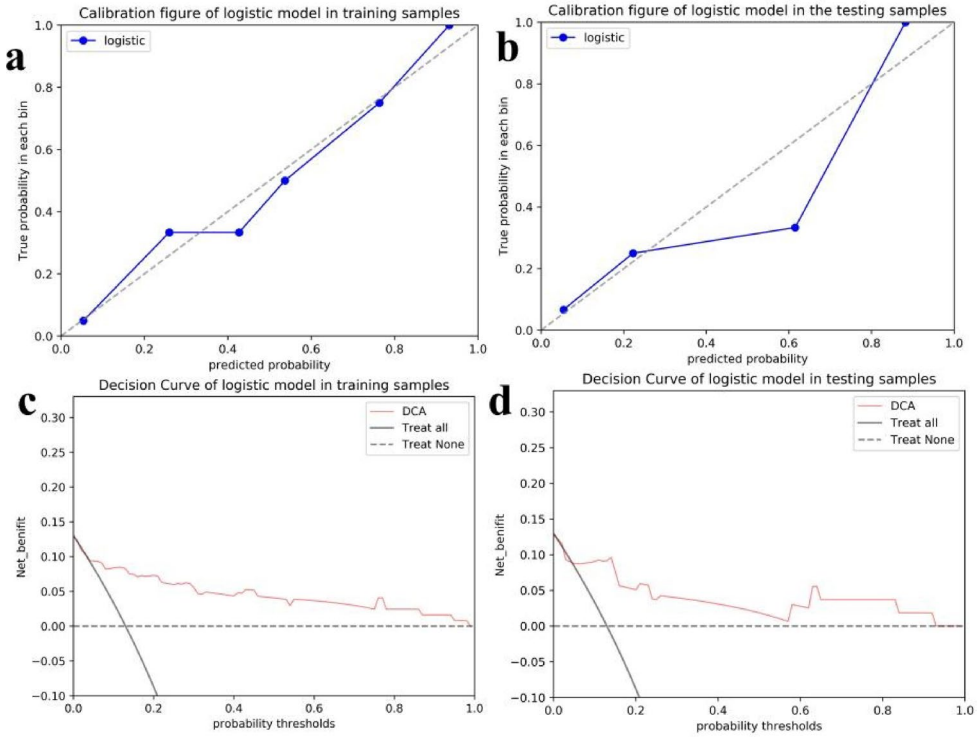

Fig. 7. Calibration curves (**a**, **b**) and decision curve analysis (**c**, **d**) of differentiation between AD and NAD BMs in the training cohort (**a**, **c**) and test cohort (**b**, **d**).

edema in the brain, and can aid in distinguishing edema in the brain and other non-tumor-related abnormal regions during tumor evaluation. Multiparametric MRI is increasingly used because it provides complementary information on the same lesion in different sequences, through integration of extracted radiomics features of different sequences separately to obtain the unique lesion information in each MRI sequence. Therefore, our method sequentially combined single sequences and achieved favorable performance. This process enhanced the results in the classification tasks for NSCLC vs. SCLC and for AD vs. NAD. Overall, the combination of T2-FLAIR + DWI + T1CE performed best in differentiating NSCLC and SCLC, with AUCs increasing from 0.632 to 0.762, respectively, and in AD and NAD identification, with AUCs increasing from 0.733 to 0.851, respectively. This finding was consistent with those from a previous MRI radiomics study on lung carcinoma classification[29], in which the best classification results were obtained for the multiparametric MRI data, with a mean AUC of 0.90 for classification between SCLC BMs and NSCLC BMs. Therefore, single MRI sequences are inclined toward overfitting, whereas multiple sequences contain complementary information that increases radiomics model robustness. In summary, the radiomic features extracted from MRI by using multiple sequences in combination provided more valuable complementary information for identifying the pathological types of lung cancer BMs, thereby offering deeper insights into the biological significance of radiomics features, and facilitating better clinical decision-making without incurring additional costs.

Similarly, Li et al.[30] have conducted a multicenter study evaluating the feasibility of a deep learning approach based on multiparametric MRI to differentiate pathological subtypes of BMs in patients with lung cancer, and achieved AUC values of 0.796 and 0.751 in distinguishing SCLC from NSCLC BMs and differentiating AD from squamous cell carcinoma BMs, respectively. Tulum et al.[31] have successfully differentiated BMs from SCLC and NSCLC (AD and squamous cell carcinoma) in small datasets (74 patients) by introducing novel radiomics features, with sensitivity and specificity values of 94.44% and 95.33%, respectively, and deep learning algorithms, with values of 94.29% and 94.08%, respectively, on the basis of T2 weighted and T2-FLAIR axial images. Those findings have demonstrated the efficiency and importance of these methods in aiding the classification of lung cancer BMs, and have indicated the proposed novel radiomics feature algorithm's substantial advantages over deep learning algorithms in identifying lung cancer subtypes in small datasets, as well as its strong interpretability. In contrast to previous studies, our research capitalized on a larger dataset and applied multiparametric MRI radiomics, which achieved AUCs of 0.762 and 0.861 in distinguishing SCLC vs. NSCLC, and AD vs. NAD BMs, respectively. Highlighting the advantages of multiparametric MRI in this context, our approach offers superior clinical visualization and interpretability to prior deep learning models[32].

Previous studies have reported that models generated from radiomics have promise in differentiating pathological types of lung cancers through BM imaging[33]. Zhang et al.[11] have demonstrated the feasibility and accuracy of radiomics features extracted from brain-enhanced CT in identifying the pathological subtypes of the primary site in the lung, thus achieving an AUC of 0.828 in differentiating primary lung adenocarcinoma from squamous cell carcinoma for patients with BMs. Although both MRI and CT are accepted as the primary

screening modalities for BMs, CT is markedly less sensitive than MRI and should be limited to patients in whom MRI is contraindicated[34]. Li et al.[14] have reported that CT radiomics-based lesion classification is highly specific in differentiating lung cancer BMs, with misclassification rates of 3.1%, 4.3%, 5.8%, and 8.1%, for SCLC, squamous cell carcinoma, AD, and large cell lung carcinoma, respectively. The authors demonstrated the feasibility of differentiating BMs from SCLC and NSCLC by using radiomics features extracted from T1CE of brain metastatic lesions to predict the pathological subtypes of the originating lung cancers. Those findings were consistent with our results, in which the predictive efficacy of the T1CE models was slightly better than that of the T2-FLAIR and DWI models, possibly because T1CE is particularly useful for demonstrating vascularity within lesions of BMs[35]. Similarly, Ahn et al.[36] have proposed that T1CE radiomics of BMs can predict the epidermal growth factor receptor mutation status of lung cancer BMs with good diagnostic performance, achieving an AUC of 89.09%. Therefore, T1CE has the potential to differentiate tumor pathological structures. T1CE not only facilitates the identification of lesion contours in BMs but also provides physicians with crucial information regarding lesion biology and treatment response[37]. Therefore, MRI has the potential to differentiate the pathological structure of tumors and to predict the pathological types of BMs in lung cancer[38].

This study has several limitations. First, the study was conducted at a single center, with an adequate overall sample size. However, the study data were skewed because of the overrepresentation of BMs originating from NSCLC and the limited number of BMs from sources other than AD, given the low incidence of NAD BMs. This imbalance decreased the generalizability of such unbalanced classification tasks, thus resulting in insufficient data for training and validating radiomics models. Furthermore, manual segmentation, although precise in delineating tumor contours, is time-consuming and labor-intensive for lesion detection and segmentation, and is susceptible to inter-observer variability. In contrast, automatic segmentation offers high reproducibility and efficiency. Specifically, automatic segmentation is considered to enable automation and elimination of human factors in ROI delineation, thereby achieving enhanced reproducibility and efficiency. However, these models must be tested on various real-world data to ensure their adaptability to diverse application scenarios. To further increase classification performance and assess clinical impact, multicenter studies using standardized imaging protocols, standardized post-processing procedures, and automatic tumor segmentation are necessary. Consequently, the sharing of multicenter, standardized, large-scale datasets and the further refinement of automated ROI segmentation methods have potential to further improve the clinical translation effectiveness of radiomics models.

Conclusion

This study demonstrated the value of using radiomics for identifying pathological subtypes of BMs in lung cancer, on the basis of preoperative multiparametric MRI. The proposed two-level stepwise binary classification radiomics models have potential to enhance current standard diagnostic imaging techniques by providing a non-invasive tool for tumor classification, thus opening greater possibilities for future research.

Data availability

The datasets used and/or analyzed during the current study are available from the corresponding author upon reasonable request.

Received: 24 October 2024; Accepted: 14 July 2025
Published online: 23 July 2025

References

1. Le Rhun, E. et al. EANO-ESMO Clinical Practice Guidelines for diagnosis, treatment and follow-up of patients with brain metastasis from solid tumours [J]. *Ann. Oncol.*, **32**(11): 1332–1347, https://doi.org/10.1016/j.annonc.2021.07.016. (2021).
2. Fecci, P. E. et al. The evolving modern management of brain metastasis [J]. *Clin. Cancer Res.* **25** (22), 6570–6580. https://doi.org/10.1158/1078-0432.CCR-18-1624 (2019).
3. Testa, U., Castelli, G. & Pelosi, E. Lung cancers: molecular characterization, clonal heterogeneity and evolution, and Cancer stem cells [J]. *Cancers (Basel)*. **10** (8). https://doi.org/10.3390/cancers10080248 (2018).
4. Nicholson, A. G. et al. The 2021 WHO classification of lung tumors: impact of advances since 2015 [J]. *J. Thorac. Oncol.* **17** (3), 362–387. https://doi.org/10.1016/j.jtho.2021.11.003 (2022).
5. Park, H. et al. Imaging of precision therapy for lung cancer: current state of the Art [J]. *Radiology* **293** (1), 15–29. https://doi.org/10.1148/radiol.2019190173 (2019).
6. Kickingereder, P., Andronesi, O. C. & Radiomics Metabolic, and molecular MRI for brain tumors [J]. *Semin Neurol.* **38** (1), 32–40. https://doi.org/10.1055/s-0037-1618600 (2018).
7. Tomaszewski, M. R. & Gillies, R. J. The biological meaning of radiomic features [J]. *Radiology* **299** (2), E256. https://doi.org/10.1148/radiol.2021219005 (2021).
8. Kniep, H. C. et al. Radiomics of brain MRI: utility in prediction of metastatic tumor type [J]. *Radiology* **290** (2), 479–487. https://doi.org/10.1148/radiol.2018180946 (2019).
9. Wang, G. et al. Radiomics signature of brain metastasis: prediction of EGFR mutation status [J]. *Eur. Radiol.* **31** (7), 4538–4547. https://doi.org/10.1007/s00330-020-07614-x (2021).
10. Chen, B. T. et al. Radiomic prediction of mutation status based on MR imaging of lung cancer brain metastases [J]. *Magn. Reson. Imaging.* **69**, 49–56. https://doi.org/10.1016/j.mri.2020.03.002 (2020).
11. Zhang, J. et al. Differentiating the pathological subtypes of primary lung cancer for patients with brain metastases based on radiomics features from brain CT images [J]. *Eur. Radiol.* **31** (2), 1022–1028. https://doi.org/10.1007/s00330-020-07183-z (2021).
12. Liu, J. et al. Multi-subtype classification model for non-small cell lung cancer based on radiomics: SLS model [J]. *Med. Phys.* **46** (7), 3091–3100. https://doi.org/10.1002/mp.13551 (2019).
13. Marentakis, P. et al. Lung cancer histology classification from CT images based on radiomics and deep learning models [J]. *Med. Biol. Eng. Comput.* **59** (1), 215–226. https://doi.org/10.1007/s11517-020-02302-w (2021).
14. Li, Z. et al. Differentiating brain metastases from different pathological types of lung cancers using texture analysis of T1 Postcontrast MR [J]. *Magn. Reson. Med.* **76** (5), 1410–1419. https://doi.org/10.1002/mrm.26029 (2016).

15. Yushkevich, P. A. et al. User-guided 3D active contour segmentation of anatomical structures: significantly improved efficiency and reliability [J]. *NeuroImage* **31** (3), 1116–1128. https://doi.org/10.1016/j.neuroimage.2006.01.015 (2006).
16. Zwanenburg, A. et al. The Image Biomarker Standardization Initiative: Standardized Quantitative Radiomics for High-Throughput Image-based Phenotyping [J]. *Radiology*, **295**(2): 328–338, https://doi.org/10.1148/radiol.2020191145. (2020).
17. Lambin, P. et al. Radiomics: the Bridge between medical imaging and personalized medicine [J]. *Nat. Rev. Clin. Oncol.* **14** (12), 749–762. https://doi.org/10.1038/nrclinonc.2017.141 (2017).
18. Lambin, P. et al. Radiomics: extracting more information from medical images using advanced feature analysis [J]. *Eur. J. Cancer*. **48** (4), 441–446. https://doi.org/10.1016/j.ejca.2011.11.036 (2012).
19. Jiang, M. et al. Radiomics based on brain-to-tumor interface enables prediction of metastatic tumor type of brain metastasis: a proof-of-concept study [J]. *Radiol. Med.* **130** (2), 190–201. https://doi.org/10.1007/s11547-024-01934-4 (2024).
20. Sun, C. et al. MR-Based radiomics predicts CDK6 expression and prognostic value in High-grade glioma [J]. *Acad. Radiol.* **31** (12), 5141–5153. https://doi.org/10.1016/j.acra.2024.06.006 (2024).
21. Jin, K. et al. Heterogeneity in primary tumors and corresponding metastases: could it provide Us with any hints to personalize cancer therapy? [J]. *Per Med.* **8** (2), 175–182. https://doi.org/10.2217/pme.10.81 (2011).
22. Dregely, I. et al. Imaging biomarkers in oncology: basics and application to MRI [J]. *J. Magn. Reson. Imaging.* **48** (1), 13–26. https://doi.org/10.1002/jmri.26058 (2018).
23. Tang, X. et al. Elaboration of a multimodal MRI-based radiomics signature for the preoperative prediction of the histological subtype in patients with non-small-cell lung cancer [J]. *Biomed. Eng. Online.* **19** (1), 5. https://doi.org/10.1186/s12938-019-0744-0 (2020).
24. Khodabakhshi, Z. et al. Non-small cell lung carcinoma histopathological subtype phenotyping using high-dimensional multinomial multiclass CT radiomics signature [J]. *Comput. Biol. Med.* **136**, 104752. https://doi.org/10.1016/j.compbiomed.2021.104752 (2021).
25. Han, Y. et al. Histologic subtype classification of non-small cell lung cancer using PET/CT images [J]. *Eur. J. Nucl. Med. Mol. Imaging.* **48** (2), 350–360. https://doi.org/10.1007/s00259-020-04771-5 (2021).
26. Wang, Y. et al. Value of radiomics model based on multi-parametric magnetic resonance imaging in predicting epidermal growth factor receptor mutation status in patients with lung adenocarcinoma [J]. *J. Thorac. Dis.* **13** (6), 3497–3508. https://doi.org/10.21037/jtd-20-3358 (2021).
27. Zhu, D. et al. Magnetic resonance imaging characteristics of brain metastases in small cell lung cancer [J]. *Cancer Med.* **12** (14), 15199–15206. https://doi.org/10.1002/cam4.6206 (2023).
28. Kaufmann, T. J. et al. Consensus recommendations for a standardized brain tumor imaging protocol for clinical trials in brain metastases [J]. *Neuro Oncol.* **22** (6). https://doi.org/10.1093/neuonc/noaa030 (2020). 757 – 72.
29. Grossman, R. et al. Differentiating Small-Cell lung Cancer from Non-Small-Cell lung Cancer brain metastases based on MRI using Efficientnet and transfer learning approach [J]. *Technol. Cancer Res. Treat.* **20**, 15330338211004919. https://doi.org/10.1177/15330338211004919 (2021).
30. Li, Y. et al. Identifying pathological subtypes of brain metastasis from lung Cancer using MRI-Based deep learning approach: A multicenter study [J]. *J. Imaging Inf. Med.* **37** (3), 976–987. https://doi.org/10.1007/s10278-024-00988-0 (2024).
31. Tulum, G. Novel radiomic features versus deep learning: differentiating brain metastases from pathological lung cancer types in small datasets [J]. *Br. J. Radiol.* **96** (1146). https://doi.org/10.1259/bjr.20220841 (2023).
32. Jiang, Y. et al. Biology-guided deep learning predicts prognosis and cancer immunotherapy response [J]. *Nat. Commun.* **14** (1), 5135. https://doi.org/10.1038/s41467-023-40890-x (2023).
33. Bekaert, L. et al. Histopathologic diagnosis of brain metastases: current trends in management and future considerations [J]. *Brain Tumor Pathol.* **34** (1), 8–19. https://doi.org/10.1007/s10014-016-0275-3 (2017).
34. Derks, S. H. A., E, Veldt, A. A. M. V. D. & Smits, M. Brain metastases: the role of clinical imaging [J]. *Br. J. Radiol.* **95** (1130), 20210944. https://doi.org/10.1259/bjr.20210944 (2022).
35. Deike-hofmann, K. et al. Sensitivity of different MRI sequences in the early detection of melanoma brain metastases [J]. *PLoS One.* **13** (3), e0193946. https://doi.org/10.1371/journal.pone.0193946 (2018).
36. Ahn, S. J. et al. Contrast-enhanced T1-weighted image radiomics of brain metastases May predict EGFR mutation status in primary lung cancer [J]. *Sci. Rep.* **10** (1), 8905. https://doi.org/10.1038/s41598-020-65470-7 (2020).
37. Young, J. R. et al. Association of lesion contour and lesion composition on MR with HER2 status in breast cancer brain metastases [J]. *Magn. Reson. Imaging.* **96**, 60–66. https://doi.org/10.1016/j.mri.2022.11.009 (2023).
38. Xiang, X. et al. Amide proton transfer-weighted MRI in predicting pathological types of brain metastases in lung Cancer [J]. *Magn. Reson. Imaging.* **108**, 59–66. https://doi.org/10.1016/j.mri.2024.01.014 (2024).

Author contributions

Conception and design of the research: LYS, XPY, and JNW. Acquisition of data: LYS. Analysis and interpretation of the data: LYS, YZ, LHX, and HM. Statistical analysis: QS and JLR. Writing of the manuscript: LYS. Critical revision of the manuscript for intellectual content: XPY and JNW. All authors read and approved the final draft.

Funding

The Postgraduate Innovation Funding Project of Hebei University (No. HBU202431).

Declarations

Competing interests

The authors declare no competing interests.

Additional information

Correspondence and requests for materials should be addressed to J.-N.W. or X.-P.Y.

Reprints and permissions information is available at www.nature.com/reprints.

Publisher's note Springer Nature remains neutral with regard to jurisdictional claims in published maps and institutional affiliations.